Large-eddy simulation of the ice shelf-ocean boundary layer near ice front of Nansen ice shelf, Antarctica

Ji Sung Na[1], Taekyun Kim[2], Emilia Kyung Jin[1*], Seung-Tae Yoon[1], Won Sang Lee[1], Sukyoung Yun[1], Jiyeon Lee[1]

[1]Korea Polar Research Institute, Incheon, 21990, South Korea
[2]Jeju National University, Jeju, 63243, South Korea

Correspondence to: Emilia Kyung Jin (jin@kopri.re.kr)

Abstract. Ice melting beneath Antarctic ice shelf is caused by heat transfer through the ice shelf–ocean boundary layer (IOBL); however, our understanding of the fluid dynamic and thermohaline physics of the IOBL flow is poor. In this study, we utilize a large-eddy simulation to investigate the role of the turbulence within the IOBL flow with sub-ice shelf plume. To resolve the different turbulence states, we impose the theoretical profile of velocity at the turbulent boundary layer by varying the power-law index. To simulate the oceanic environment near Nansen ice shelf, boundary conditions by the melting at the ice shelf base and the freezing at the sea surface are based on *in situ* observations. Then, we compare the simulation results and observation data. In terms of thermohaline circulation near the ice front, and the vertical distribution of temperature and salinity, which is determined by the positively buoyant meltwater created from the ice shelf base near the ice front, we conclude that the IOBL flow near the ice front is realistically resolved. In the strong turbulence case, distinct features are present in the high momentum of meltwater with a strong Ekman layer and the large scale of the baroclinic eddies. Compared to the weak turbulence case, the strong turbulence case exhibits 66% increase in basal melting with high-speed currents. This demonstrates that the larger baroclinic eddies enforces heterogeneous distribution of positively buoyant meltwater upwelling. The findings of this study contribute to the investigations on the complex features of IOBL flow and its impact on ocean circulation.

1 Introduction

The Antarctic ice sheet (AIS) is buttressed by floating extensions of land ice and ice shelves (Rignot et al., 2013). One of the important roles of ice shelves in controlling the mass balance of the AIS is to hinder the flow of inland ice into the ocean to prevent sea level rise (Holland et al., 2020). Internal glaciological stresses, iceberg calving and surface melting at the sub-ice shelf may be key contributors to weakening the stability of ice shelves (Liu et al., 2015; Smith et al., 2020). However, acquiring direct access to the ocean-filled cavities beneath ice shelves from the open ocean via autonomous underwater vehicle (e.g., Jenkins et al., 2010) or through the ice shelf by hot-water drilling (e.g., Stanton et al., 2013) requires challenging intermediate to large-scale logistical support depending on the size and thickness of the ice shelves.

The sub-ice shelf oceanic environment can be divided into two classes, namely the "cold-water cavity" (e.g., the Larsen C, Ross, Filchner-Ronne, and Amery ice shelves) and the "warm-water cavity" (e.g., the Getz and Totten ice shelves),

depending on the amount of basal melting and ocean conditions (Gwyther et al., 2016; Joughin et al., 2012). Shear force generated by tidal mixing and the thermohaline process during sea ice formation are the basal melting driving forces in cold water cavity (e.g., high salinity shelf water), whereas the intrusion of circumpolar deep water (CDW), which is the water well above the local freezing temperature, is the main driving force for basal melting in the warm-water cavity (Davis and Nicholls,

35   2019; Jacobs et al., 1992; Yoon et al., 2020). The ice shelf–ocean boundary layer (IOBL), which is the boundary layer (meters to tens of meters) right beneath the ice shelf, is difficult to investigate because the shear forces from the ocean and stabilizing force of the meltwater combine within the IOBL (Begeman et al., 2018; Naveira Garabato et al., 2017). Therefore, the IOBL flow and its structure need to be investigated with a turbulence resolving model to reveal the basal melting physics below ice shelves (Jenkins, 2016; Holland et al., 2020).

40   Various observational efforts have been performed in main ice shelves of Antarctica to observe thermohaline characteristics and its structure within IOBL and ocean condition beneath the ice shelve (Jenkins, 2010; Kimura et al., 2015). In Larsen C ice shelf which is one of cold-water cavity, well-mixed feature (20 ~ 30 m) of temperature and salinity induced by strong tidal forcing and weak stratification structure was observed, showing that it could yield moderate melt rate, despite the low thermal driving (Davis and Nicholls, 2019). Similar melt rates for weak stratification were also observed beneath the

45   Fimbul and Ross ice shelves (Arzeno et al. 2014; Hattermann et al., 2012). Moreover, the heat entrainment is prevented near the grounding line of the Ross ice shelf due to the strong density gradient between meltwater and denser continental shelf water in this region, yielding a low melting. (Begeman et al., 2018).

Positively buoyant sub-ice shelf plumes created near the grounding line can affect the stratification and heat entrainments within the IOBL; they yield the shear because of the buoyant moving of meltwater near the grounding line and ice shelf front

50   (Hewitt, 2020; Holland and Jenkins, 1999). Since the sub-ice shelf plume modulates the IOBL characteristics with strong shear mixing, the basal melt rate can be increased by weakening the stratification and enhancing the entrainment of seawater from the outer region. At the ice shelf bottom near the ice front, increased turbulent mixing can increase the IOBL thickness, leading to changes in heat exchange and entrainment with melt rate modification (Jenkins, 2011).

Despite the various observational efforts, the thermohaline physics as well as the turbulent environment for the melting

55   and refreezing processes within the IOBL remain unclear. The challenges in elucidating the afore-mentioned primarily stem from technical difficulties in accessing and observing the sub-ice shelf ocean cavity, particularly the IOBL and the complexity of the flow itself, which has highly turbulent and buoyant characteristics with various spatial and temporal scales (Nicholls et al., 2016; Everett et al., 2018). To clearly determine the effects of various forcing (e.g. shear, stabilizing force of the meltwater and buoyant moving of meltwater), independent experiments or observations for the forcing are needed. Therefore, there are

60   growing demands for dealing with this highly complex physics, which has led researchers to introduce high-resolution turbulence models such as the large-eddy simulation (LES) or direct numerical simulation (DNS) which have more realistic boundary conditions constrained by *in situ* observations (Gayen et al., 2016; McConnochie and Kerr, 2018; Mondal et al., 2019; Vreugdenhil and Taylor, 2019).

The LES has been successfully applied to investigate the role of turbulence in the ice shelf–ocean interaction within the IOBL for cases in Greenland (Carsey and Garwood, 1993; Denbo and Skyllingstad, 1996) and the Arctic Sea (Glendening, 1995; Skyllingstad and Denbo, 2001; Matsumura and Ohshima, 2015; Ramudu et al. 2018; Li et al. 2018). However, applications of the LES to IOBL at sub-ice shelf environment are quite limited.

In this study, we performed LES experiments for the IOBL and oceanic flow including freezing effect at sea surface and the basal melting process with neutrally buoyant sub-ice shelf plume near ice front. Boundary conditions used in LES were made based on *in situ* observation data—namely conductivity-temperature-depth (CTD), lowered acoustic Doppler current profiler (LACDP), automatic weather station (AWS) data—collected in front of the Nansen Ice Shelf (NIS), cold-water cavity, during the Antarctic expedition led by the Korea Polar Research Institute in January and February 2017. The main parameter in the LES experiments was turbulence intensity within IOBL. For consistency in experiments, we considered different turbulence state while keeping the same thermohaline forcing by the melting and freezing. The main objectives of this study are to examine the physics within the IOBL in this NIS region and to determine the impacts of turbulence on the basal melting at the ice shelf bottom. Using the validated three-dimension outputs from LES, we were able to account for distribution of melting at ice shelf bottom and detailed physics including turbulent characteristics, changes in fluxes within IOBL.

Section 2 of this paper presents the governing equations (i.e., the Navier–Stokes equation and liquidus condition) for the oceanic flow with the melting and freezing effects as well as a detailed explanation of the simulations. Section 3 provides an overall analysis of the simulations for validating the LES results and determining the characteristics within the IOBL—flow velocity, potential temperature, salinity, fluxes, and turbulence statistics. Primary findings, future works, and implications of this study are summarized in Sections 4 and 5.

2 Methodology

2.1 Numerical model

To simulate the oceanic flow with refreezing, the parallelized large-eddy simulation model (PALM, version 6–r4536) developed by Leibniz University was employed (Noh et al., 2009; Raasch et al., 2001). This model solves the non-hydrostatic, Boussinesq-approximated, filtered Navier–Stokes equations with buoyancy force, Coriolis force, and subgrid-scale (SGS) turbulent closure. The Boussinesq approximation can be applied to flows with negligible density variation. Furthermore, in the time integration, the time-difference formulas were computed using the third-order Runge–Kutta method. The 5th order upwind scheme was used to solve the flow advection (Wicker and Skamarock, 2002). The pressure was modeled using a Poisson equation, while the mass, momentum, potential temperature, and salinity conservations were governed by Eqs. (1)–(4), respectively.

$$\frac{\partial \overline{u_k}}{\partial x_k} = 0 \, , \tag{1}$$

<center>3</center>

95 $\quad \frac{\partial \overline{u_i}}{\partial t} + \frac{\partial \overline{u_i u_k}}{\partial x_k} = -\frac{1}{\rho}\frac{\partial \overline{\pi^*}}{\partial x_k} - \varepsilon_{ijk}f_j\overline{u_k} + \varepsilon_{i3k}f_3\overline{u_{g,k}} + g\frac{(\rho_\theta - <\rho_\theta>)}{<\rho_\theta>}\delta_{i3} - \frac{\partial \tau^r_{ki}}{\partial x_k},$ $\qquad\qquad$ (2)

$\tau^r_{ki} = \tau_{ki} - \frac{1}{3}\tau_{jj}\delta_{ki}, \overline{\pi^*} = \overline{p^*} + \frac{1}{3}\tau_{jj}\delta_{ki},$

$\frac{\partial \overline{\theta}}{\partial t} = -\frac{\partial \overline{u_k \theta}}{\partial x_k} + \frac{\partial H_k}{\partial x_k} + Q_\theta,$ $\qquad\qquad$ (3)

$\frac{\partial \overline{Sa}}{\partial t} = -\frac{\partial \overline{u_k Sa}}{\partial x_k} + \frac{\partial S_k}{\partial x_k} + Q_{sa},$ $\qquad\qquad$ (4)

where u_k is the flow velocity, ρ is the seawater density, π^* is the dynamic pressure, ε_{ijk} is the Levi–Civita symbol, f is the
100 Coriolis force for 75S ($-1.41 \times 10^{-4}\,\mathrm{s}^{-1}$), δ_{ij} is the Kronecker delta function, g is the gravitational acceleration, ρ_θ is the potential density, T is the absolute temperature, v is the dynamic viscosity, τ^r_{kj} is the Reynolds stress, θ is the potential temperature, p is the hydrostatic water pressure, p_0 is the reference pressure, and Sa is the salinity (Jackett et al., 2006). Additionally, Q_θ and Q_{sa} are the external forcing of the source/sink terms of T and Sa, respectively. Overbars denote that the values have been filtered over the grid volume. Combining these equations, the SGS turbulent kinetic energy (e) equation can be derived as
105 follows:

$\frac{\partial \bar{e}}{\partial t} = -\overline{u_k}\frac{\partial \bar{e}}{\partial x_k} - \tau_{ki}\frac{\partial \overline{u_i}}{\partial x_k} + \frac{g}{\theta_0}\overline{u'_3\rho'_\theta} - \frac{\partial}{\partial x_k}\overline{\{u'_k(e + \frac{p'}{\rho_0})\}} - \varepsilon$ $\qquad\qquad$ (5)

where $= \frac{\overline{u_i}\overline{u_i}}{2}$, and ε is the SGS dissipation rate.

The SGS stresses for the momentum, potential temperature, and salinity are parameterized as follows: (Maronga et al., 2015)

$\tau_{ki} = \overline{u_k u_i} - \overline{u_k}\,\overline{u_i} = -K_m\left(\frac{\partial \overline{u_i}}{\partial x_k} + \frac{\partial \overline{u_k}}{\partial x_i}\right) + \frac{2}{3}\delta_{ik}\bar{e},$ $\qquad\qquad$ (6)

110 $H_k = \overline{u_k\theta} - \overline{u_k}\bar{\theta} = \overline{u'_k\hat{\theta}} = -K_h\left(\frac{\partial \overline{\theta}}{\partial x_k}\right),\quad K_h = \left(1 + 2\frac{l}{\Delta}\right)K_m,$ $\qquad\qquad$ (7)

$S_k = \overline{u_k Sa} - \overline{u_k}\overline{Sa} = \overline{u'_k Sa'} = -K_h\left(\frac{\partial Sa}{\partial x_k}\right),$ $\qquad\qquad$ (8)

$\frac{\partial}{\partial x_k}\left[\overline{u'_k(e + \frac{p'}{\rho_0})}\right] = -\frac{\partial}{\partial x_k}v_e\frac{\partial \bar{e}}{\partial x_k}, v_e = 2K_m,$ $\qquad\qquad$ (9)

$\varepsilon = C_\varepsilon \frac{e^{3/2}}{l}, \quad C_\varepsilon = 0.19 + 0.74l,$

$K_m = C_m l\sqrt{\bar{e}}$ with empirical value $C_m = \text{constant} = 0.1$, and $l = \min(1.8z, \Delta, 0.76\sqrt{\bar{e}}[\frac{g}{\rho_{\theta,0}}\frac{\partial \overline{\rho_\theta}}{\partial z}]^{-\frac{1}{2}})$

115 where l is the turbulent mixing length (depends on wall distance, grid spacing and stratification), Δ is the length scale of the filter and ρ_θ is potential density.

It is necessary to determine ambient variables (θ_f and S_f) within the IOBL and interfacial variables (θ_b and S_b) near the ice shelf–ocean boundary to resolve the thermal and salinity changes by the freezing effect at sea surface or basal melting effect at the ice shelf–ocean boundary. Herein, we determined the ambient variables based on *in situ* CTD observations. To obtain
120 interfacial variables, we solved the conservation equations of heat and salt, along with the liquidus condition and turbulent transfer coefficients for heat and salt (Beckmann and Goosse, 2003; Vreugdenhil and Taylor, 2019).

4

$$c_w \rho_w \Gamma_\theta u_*(\theta_f - \theta_b) = \rho_i L_i m \,, \tag{10}$$

$$\rho_w \Gamma_S u_*(S_f - S_b) = \rho_i S_b m \,, \tag{11}$$

$$\theta_b = \lambda_1 S_b + \lambda_2 + \lambda_3 P \,, \tag{12}$$

$$S_b = \frac{-\left(\theta_b + \frac{L_i \Gamma_S}{c_w \Gamma_\theta}\right) + \sqrt{\left(\theta_b + \frac{L_i \Gamma_S}{c_w \Gamma_\theta}\right)^2 - 4\lambda\left(\frac{L_i \Gamma_S}{c_w \Gamma_\theta}\right)S_f}}{-2\lambda} \,, \tag{13}$$

where m is the melting rate at the ice shelf base or the freezing rate at the sea surface, the subscript w refers to parameters for water and the subscript i refers to parameters for ice. The parameters values are listed in Table 1. The friction velocity at the ice shelf base was calculated from the simulated velocity field in four different cases. In all cases, the constant friction velocity calculated from wind speed and its stress at sea surface was used.

The fluxes for temperature and salinity, $q_{\theta*}$ and q_{S*} at the ice shelf bottom are formulated by Monin-Obukhov similarity and interfacial values, θ_b and S_b obtained by resulting equation, Eq (13) (McPhee et al., 1987; Ramudu et al. 2018).

$$q_{\theta*} = \frac{1}{\Gamma_\theta}[\theta(z_1) - \theta_b]u_* \,, \tag{14}$$

$$q_{S*} = \frac{1}{\Gamma_S}[S(z_1) - S_b]u_* \,, \tag{15}$$

$$\tau_{\theta,S} = \frac{1}{\kappa}\ln\left(\frac{z_1}{z_0}\right) + 1.57\left(\frac{u_* z_0}{v}\right)^{1/2}\left(\frac{v}{k_{\theta,S}}\right)^{2/3} \,, \tag{16}$$

where u_* is the friction velocity which is calculated by the velocity at first node and roughness length. Γ_θ, Γ_S are non-dimensional transfer coefficients of heat and salt, which are determined by the near-wall turbulence physics. These fluxes for the melting and the freezing rates were applied at the first grid from the ice shelf base or sea surface. In this study, the lateral melting at the ice shelf front is not included based on assumption that the lateral melting is negligible because of extremely low thermal driving at the lateral side of the ice shelf front.

2.2 Simulation description

In this study, we conducted four LES simulations corresponding with the turbulence state within the IOBL to reveal the role of the turbulence on IOBL characteristics. Different turbulence states were described in four different vertical profiles of zonal velocity. Based on the power-law assumption of turbulent boundary layer flow ($U=U_t (z/z_0)^{(1/n)}$), different velocity profiles were composed via different power-law indices, n = 3 (weak turbulence), 4, 5 and 7 (strong turbulence) to resolve the turbulence intensity within IOBL (Irwin, 1979; Kikumoto et al., 2017). These velocity profiles for the four different cases were used at the initialization of the flow field and inlet boundary condition. The freestream (geostrophic) velocity U_t was set as 0.06 m s^{-1}, based on *in situ* observation near the ice front. The simulation dimensions were 3456 m × 3456 m × 864 m in the x, y, and z directions, respectively. For the simulations, a grid of 288 × 288 × 144 cells was used with a 12m horizontal grid and a 6 m vertical grid with a surface roughness (z_0) of 0.005m (Gwyther et al., 2016). The grid size and surface roughness used were based on a numerical study of high shear plume flow (Gao et al., 2019). In addition, we performed the grid sensitivity study for grid size, in terms of result accuracy and computational cost (Figure S1 in Supplementary). Through the grid

independent study, we concluded that this moderate grid resolution ($288 \times 288 \times 144$) was proper in resolving turbulence with the parameterization of melting and freezing effects. Using masking method, an idealized ice shelf with a depth of 280 m was placed in the upper-left part of the simulation domain, referring to the ice shelf depth near the ice front of the NIS (Briscolini

155 and Santangelo, 1989; Stevens et al., 2017). For zonal velocity, potential temperature, and salinity, the inlet boundary condition was set to the Dirichlet boundary condition with constant vertical profiles that were the same as the initial profiles. At the start of the simulation, initial profiles were imposed on the whole domain. Initial profiles were set in the variation range of vertical profiles of our 24 CTD and 23 LADCP observations conducted near the ice front of the NIS. The outlet boundary condition was determined to match the radiation boundary condition (extrapolation), which prevented numerical errors without rapid

160 change of velocity and scalars. The cyclic boundary condition was applied to lateral boundaries, while a Dirichlet boundary condition ($U_{top} = 0$ m s^{-1}) was imposed on the top layer. Zero velocity at the sea surface implies the exclusion of the wind effect to examine the ocean dynamics caused by the sub-ice shelf plume solely. A random generator for small velocity perturbation was applied at depths from 30 to 800 m to quickly spin up the turbulence. The total simulation time required to reach the quasi-steady state was 96 hours. Detailed information about the simulation domain and boundary conditions is summarized in Fig.

165 1. This figure shows the target research region, observation points, and simulation domain with a schematic diagram for the oceanic flow alongside a sub-ice shelf plume. We configure two physical domains in modelling referring to sub-ice shelf and ocean regions. In the ocean region, simulated ocean velocity, potential temperature, and salinity of the LES results were validated with CTD and LADCP observations. Then, detailed flow characteristics of the IOBL flow beneath the ice shelf were investigated.

170

2.3 CTD, LADCP observations

During the hydrographic survey conducted from 26 January to 15 February 2017 by the icebreaking research vessel ARAON operated by the Korea Polar Research Institute, full-depth CTD and LADCP profiles were obtained with one-hour intervals from 14 February 2017 13:00 UTC to 15 February 2017 11:55 UTC at a single site in the Terra Nova Bay in front of

175 the NIS in order to examine the vertical structures of sub-ice shelf plume with temporal variations. The exact location of the observations is 75.008 °S, 163.617 °E (Fig. 1b). The observation location is approximately 1 km away from the ice front. Because the LADCP data was incorrectly observed at the final casting, 24 CTD profiles and 23 LADCP profiles were used in this study. The CTD data were processed following the SBE recommended procedure (Sea-Bird Electronics, Inc., Bellevue, Washington, USA; 2014) and the LADCP data were processed using the methods introduced in Thurnherr (2004). Atmospheric

180 properties such as wind speed, temperature, sensible heat and frazil ice formation (Thompson et al., 2020) was obtained from the AWS instrument on ARAON and it is list-up in Table 1. The detailed shipboard information and processing methods for the hydrographic data are described in Yoon et al. (2020).

3 Results

3.1 Validation of simulation results

To confirm that the IOBL and oceanic flows approach a quasi-steady state, we plotted the time series of friction velocities at the ice shelf bottom (Figure 2). In this study, we determined the IOBL region to the depth where the heat flux was 5% of maximum heat flux near the ice shelf base as IOBL physics is analogous to the atmospheric boundary layer (Derbyshire, 1990). Detailed analysis of the IOBL top is discussed at later analysis for the vertical heat flux profile. The total simulation time (96 h) is normalized by large-eddy turnover time (t^*) which is calculated by the scale of overturning large eddy within the IOBL divided by the friction velocity. Friction velocities in four LES cases greatly fluctuated during the whole period, showing there are large-scale eddies beneath the ice shelf. Friction velocity fluctuation due to large-scale eddies shows a repetitive pattern after 14 t^*. As the turbulence near the IOBL is stronger, the large-scale eddy corresponding to the Rossby radius of deformation is larger (Figure S2). The averaged friction velocities for n = 3, 4, 5 and 7 are 0.00169, 0.00208, 0.00255 and 0.00283 m s^{-1}, respectively. This difference is due to the different amount of momentum entrainment by the turbulence intensity within the IOBL. Table 2 presents these friction velocities and the large-eddy turnover times for the four cases. We calculated the time-averaged results within 3 t^* period in the later analysis to capture the averaged features of the flow without temporal variance.

Figure 3 illustrates vertical sections (y = 1,728 m, domain center) of zonal velocity, potential temperature, and salinity which are time-averaged in 3 t^* period to examine the spatial distributions of flow structures and variables in two extreme cases (n=3, n=7) for turbulence intensity. In the ocean region, velocities in cases with weak and strong turbulence had similar patterns for two ocean circulations in the upper ocean region (0–280 m depth). In this study, we refer to these circulations as the "ice front circulations". Since we did not impose the wind effect at the top boundary, we can conclude that the development of outer circulation is mainly induced by the downward force (convective mixing) of the salt flux by sea ice formation as well as the shear stress by the momentum difference between the upper region and sub-ice shelf plume. Moreover, the development of the inner circulation is mainly due to the upwelling of the buoyant water and the downward force of the salt flux. Thus, the inner circulation is stretched in the vertical direction, whereas the outer circulation is stretched in the horizontal direction. The downward force that the two circulations share pushes the sub-ice shelf plume, moving the stratification line (280 m depth) near the ice shelf to about 350 m depth. A noticeable difference between the two cases is observed near the ice front and beneath the ice shelf. At depths from 280 to 320 m (IOBL region), high zonal velocity beneath the ice shelf is observed in the strong turbulence case (n = 7). After passing the ice shelf, this high-speed current flows in the perpendicular direction to the ice front. In the weak turbulence case (n = 3), a relatively low velocity is observed beneath the ice shelf and the current rises after passing the ice shelf. These momentum differences in the two cases mainly affects the magnitude and scale of the ice front circulations. Positive buoyancy is originated from the meltwater created at the ice shelf base near the ice front. In this study, we refer to this water as the "positively-buoyant, ice shelf water (PISW). In contrast to the sub-ice shelf plume which has neutral buoyancy near the ice front, PISW has strong buoyancy. PISW is a major contributor to the formation of inner ice front circulation. Because the temperature of the sub-ice shelf plume is higher than a local freezing temperature at 280m depth,

vigorous basal melting occurs and creates PISW. At zonal distances from 1280m to 1600m, this PISW mixes with the outer ocean and has about –2°C of potential temperature, rising along the ice front edge. The same feature is clearly observed in salinity distribution. Another noticeable difference between the two cases is temperature and salinity in upper ocean region. In a strong turbulence case, increased friction velocity affects the increment of the basal melting and large amount of PISW, forming low temperature and salinity in the upper ocean region. Below 400 m depth, a well-stratification features appear in salinity distribution. These results entail that the sub-ice shelf plume has quasi-neutral buoyancy with little upward forcing.

For validation, we plot the vertical profiles of the stream-wise zonal velocity, potential temperature, and salinity in the LES results and CTD and LADCP observations to quantitatively compare the vertical distribution of the momentum and variables related to potential density (Figure 4). For the initial and inlet boundary conditions of velocity, the theoretical power-law profiles (inset plot in Figure 2) below 280m and zero velocity above 280m were set to examine the cause of ice front circulation development which is observed in CTD, LADCP observations. For the initial condition and the inlet boundary condition of temperature and salinity, the sub-ice shelf plume is located at depths from 280 to 550 m. In the velocity profiles, the LES results with varying turbulence states well resolve with the development of the ice front circulation in the 23 LADCP profiles, although it has a difference in velocity magnitude of negative velocity near the sea surface. This difference is from the difference in downward forces between our simulation and in reality. As previously mentioned, a difference in IOBL current perpendicular to the ice front is also observed in this plot. The potential temperature and salinity profiles of those four LES results agree with the 24 CTD profiles, in terms of magnitude and the depth of peak values. Due to a difference in melting rate, the magnitudes of potential temperature in the upper mixed layer in the cases are quite different: in the upper mixed layer, the potential temperature in four cases are about –1.925, –1.93, –1.932, –1.943°C, respectively. This difference is due to the amount of PISW created from the ice shelf base near the ice front. Similar features with the effect of PISW are also observed in salinity profiles. There are two interesting things that are difficult to explain in observations. One of them is why the sub-ice shelf plume is located below 400 m depth even though the ice shelf base is located at 280 m depth. The LES results show that the downward force of the salt flux and the development of the inner ice front circulation (Figure 3) push the stratification line near the ice shelf. Second is the existence of relatively low-temperature water (–1.96 °C) at 100 m depth. This feature can be explained by the PISW upwelling process. Through the comparison of quantity and its characteristics, we conclude that the LES results are similar to the *in situ* observations of oceanic environments, in terms of the physical process of ocean circulation and the magnitude of the main variables.

In the LES model, the filtered Navier–Stokes equation is solved with the modelled effect of small-scale eddies to reduce computational cost. Therefore, the criteria for "small-scale" are important; these criteria are determined by grid size. To evaluate grid size and modelling of small-scale eddies in this study, it is necessary to confirm that the turbulence characteristics of the LES result are similar to the turbulence characteristics of inertial subrange in which energy cascading occurred with few dissipations. The one-dimensional turbulence energy spectra at 291 m depth (within IOBL) in the cases with weak and strong turbulence are plotted in Figure 5. Moreover, we examine different zonal locations (x = 400, 800, 1200, 1800, 2300 and 2800 m) to observe a spatial transition of the IOBL flow. For a wavenumber greater than 0.002033 m^{-1} which represents the

approximately 500 m scale of the energy-containing eddy, the energy spectra of the LES results follow the –5/3 slope of the Kolmogorov scale in the inertial subrange. For the cases with weak and strong turbulence, a similar trend of spatial transition of energy spectra at the IOBL region is observed. At zonal distance of 400 and 800 m, turbulence is under a fully-developed state with a similar magnitude of energy spectra. Near the ice front (1200 m) and right after passing the ice front (1800 m), the turbulence energy spectra are suppressed by the inner ice front circulation and downward forcing. At the region of the outer ice front circulation, the turbulence energy spectra exhibits the highest energy level.

To examine the pathway and destination of PISW, we illustrate the horizontal distributions of 3 t^* time-averaged freezing rate at the sea surface, as shown in Figure 6. Because the interfacial temperature and salinity determined by atmospheric forcing and friction velocity by wind stress are the same in four cases, the difference in freezing rate comes only from ocean conditions. Although the melting rate is low, and the amount of PISW is small in the weak turbulence case, most of its PISW is rising along the ice front owing to low flow momentum. Otherwise, some of the PISW in the strong turbulence case is also rising along the ice front, but most of them are advected to the upper mixed layer apart from the ice shelf. As a result, different patterns of freezing rate is observed in two cases. In the weak turbulence case, most of the freezing rate is concentrated right after the ice shelf, having a maximum freezing rate of 8.9 m yr^{-1}. Although a maximum freezing rate of 7.16 m yr^{-1} is observed right in front of the ice shelf in the strong turbulence case, the spatial-averaged freezing rate is higher than that in the weak turbulence case. An interesting point in the strong turbulence case is a heterogeneous pattern of freezing rate in the meridional direction. This feature is highly related to its perturbation scale of the outer ocean (Rossby radius of deformation) and PISW upwelling (Figure S2). In the weak turbulence case, PISW upwelling occurs along the ice front edge, comprising a strong, narrow PISW layer near the ice front with strengthened inner ice front circulation and this blocks an intrusion of the outer ocean with baroclinic eddy. However, it is observed the heterogeneous patterns of PISW and freezing rate in strong turbulence case, because the PISW layer near the ice front is wide and weak, permitting the intrusion of the outer ocean with large baroclinic eddy.

3.2 IOBL characteristics in the sub-ice environment

The afore-mentioned analysis shows that the LES model adequately resolves the oceanic flow beneath the ice shelf with the thermohaline dynamics, such as IOBL dynamics, PISW upwelling and convective mixing by salt flux at the sea surface. Next, we explore the flow characteristics of the IOBL beneath the ice shelf using the validated LES results. Since we assumed a flat base of the ice shelf in this study, the buoyant force of PISW does not accelerate the PISW at the ice shelf base. Driving forces within the IOBL flow are shear forces caused by the momentum of the sub-ice shelf plume and the stratification force (stabilizing force) caused by the PISW. In this section, we comprehensively analyze the oceanic flow characteristics to reveal the relation between the flow physics and melting patterns within the IOBL beneath the ice shelf.

Figure 7 illustrates the horizontal distributions of 3 t^* time-averaged meting rate at the ice shelf base. As shown in Fig. 7, the different magnitudes of melting rates are observed in cases with weak and strong turbulence. Except magnitude of melting

rate, the overall trend in two different turbulence cases is similar. In the region close to the inlet boundary and ice front, the melting rate is high. Because inlet boundary conditions are theoretical profiles, the transition for fully developed IOBL flow is needed. As shown in Figure S2 in supplementary, turbulence intensities in weak and strong turbulence cases are fully developed after 312m, 336 m distance, respectively. Therefore, we exclude the region for non-developed turbulence in the analysis. The high melting rate in the region close to the ice front is evidence of an interaction with the upper ocean and ice front circulations. Averaged values in two different turbulence cases are 0.092 and 0.153 m yr^{-1}, respectively, having a 66% difference in the melting rate near the ice front, NIS. The melt rate for the strong turbulence case is quite low (1.74 fold) compared to the observed melt rate (0.42 m yr^{-1}) proposed by the study of Wray (2019), which is about basal channel near the NIS front. However, the melt rate in our LES results is comparable to the observed melt rate, considering the change of heat transfer coefficient by thermal driving and the difference of thermal driving (0.032°C in our LES simulations and 0.14°C in the study of Wray (2019)). The heterogeneous patterns of melting rate in the meridional direction (parallel direction to the ice front) are not noticeable.

To observe and quantify the high-speed current at IOBL in the strong turbulence case and Ekman layer development, we plot vertical profiles of velocities, turbulence intensity and horizontal momentum flux beneath the ice shelf (Figure 8). At 280–400m depths, the zonal velocities exhibits quite different structures for the four cases. The strong turbulence case displays the smallest mean shear gradient but the largest turbulence intensity, whereas the weak turbulence case has an opposing features. Since the turbulence kinetic energy production is proportional to the mean shear gradient and turbulent shear stress (Pope, 2000), turbulent shear stress is the highest in the strong turbulence case, showing that the turbulent shear stress has a large portion of turbulent kinetic energy production. Due to high turbulent shear, a strong Ekman layer with negative meridional velocity (flows to the right of geostrophic flow) develops within the IOBL. This feature is also observed in the horizontal momentum flux. Above the depth of the IOBL top, a positive meridional velocity is observed. This is because the intrusion of the outer ocean with baroclinic eddies affects on this region. Moreover, the Ekman layer depths for the weak and strong turbulence cases are 11 m and 17 m, respectively. These depths are comparable to the estimated depths (11.9 and 19.6 m, respectively) based on friction velocity and the Coriolis parameter (Coleman, 1990).

Figure 9 shows the vertical profiles of the vertical fluxes of momentum and heat beneath the ice shelf. As shown in Figure S4 which depicts the vertical buoyancy flux profiles, PISWs in both weak and strong turbulence cases have a stabilizing effect because of its positively buoyant characteristic. Moreover, PISW in the weak turbulence case has more buoyancy than that in the strong turbulence case because of the momentum difference between the PISWs in the two cases. Subsequently, we determine the PISW top (297 m). Combining the regions where the meltwater and its stabilizing effect dominated with the region where heat entrainment by turbulence was vigorous (5% of maximum heat flux), the IOBL top is determined. In the strong turbulence case, the vertical momentum flux is negative and its maximum is located within IOBL (IOBL top - 319 m depth). This implies that the momentum entrainment from the sub-ice shelf plume to IOBL is effective, having large heat entrainment. However, the depth of maximum negative flux in the weak turbulence case is located at 347 m, slightly away from the IOBL. This difference causes the difference in heat flux magnitude at the PISW top. Negative heat flux at 320–400

m depths denotes that some of the entrained heat by the intrusion of the outer ocean is transferred to the downward direction. For steady basal melting, positive heat flux has to remain within the IOBL through flow advection penetrating the stratified IOBL. The maximum positive heat flux for the weak and strong turbulence cases is 138, 213 W m^{-2}, respectively, with a 54% difference. This difference is comparable with a difference (66%) in the melting rate near the ice front, confirming that basal melting is proportional to the amount of heat flux and entrainment by flow advection penetrating the stratified IOBL.

4 Discussions

4.1 LES simulation for IOBL flow

The main processes of the ice–ocean interactions related with ice mass balance in the cold-water cavity are basal melting near the grounding zone and refreezing near the ice front (Dinniman et al., 2016; Jacob et al., 1992; Petty et al., 2013). One of these processes is triggered by the intrusion of the High Salinity Shelf Water (HSSW). When this dense seawater intrudes into the ocean-filled cavity beneath the ice shelf, the base of the deep ice shelf is melted because the temperature of the HSSW is higher than the freezing temperature at this depth. Then, super-cooled, less-dense water is formed at the base of the deep ice shelf and rise, creating the sub-ice shelf plume with high momentum and buoyancy. As the plume gets closer to the ice front, it flows outward, losing its buoyancy. Near the ice front, basal melting can occur due to heat entrainment from a relatively warm, sub-ice shelf plume or the interaction with the upper mixed layer. This basal melting creates meltwater which has positively buoyant characteristics (PISW in this study).

During these processes, the IOBL flow and its turbulence structures have a crucial role in mass and energy transport in Antarctic oceanic flow. Additionally, these structures are key to explaining and evaluating the complex phenomenon of ice–ocean interaction beneath the ice shelf. Therefore, it is necessary to investigate the detailed structures and their physical processes to follow the trajectory of mass and energy. Understanding the flow physics and structures using only the one-dimensional profile obtained by CTD and LADCP has many limitations. Moreover, the observational approach is difficult in sub-ice shelf environments. As shown in previous LES studies of ice–ocean boundary (Ramudu et al., 2018; Vreugdenhil and Taylor, 2019), the LES model is a powerful tool for resolving the flow and its three-dimensional structures with the change of mass and energy, with high accuracy and low computational cost. Therefore, employing the numerical approach such as a regional ocean model, including the LES is one of the solutions for resolving the three-dimensional structures in the oceanic flow. Under these circumstances, we demonstrated one methodology to investigate the IOBL physics and ocean dynamics by combining the numerical approach with the observational effort. In this study, we used the LES model with *in-situ*-based boundary conditions to expand the one-dimensional observation profile in the oceanic region to the three-dimensional flow-field in the oceanic region and the sub-ice shelf region. Additionally, we set ambient values (θ_f, S_f) by using the CTD results to obtain the interfacial values (θ_b, S_b) in the liquidus condition. In this study, we performed an evaluation of this methodology, validating our results in terms of ocean circulation, trend, and magnitude of temperature and salinity. In future work, this methodology will be validated using multi-dimensional sub-ice shelf observations such as the autonomous underwater vehicles

11

350 (AUV), glider instruments, etc. Moreover, boundary conditions for the sub-ice shelf region and sea ice formation through sea surface and salt flux change by precipitation and evaporation will be investigated for simulating the IOBL and oceanic flow more realistically. Furthermore, the effect of frazil ice dynamics (e.g. crystal growth rate, nucleation and gravitational removal) in sea surface or marine ice should be investigated because the change in plume characteristics and amount of temperature and salinity is highly related with frazil ice dynamics (Galton-Fenzi et al., 2012; Rees Jones and Wells, 2018).

355

4.2 IOBL characteristics in the sub-ice environment

The characteristics of the IOBL are more complex than the oceanic characteristics in the upper mixed layer since heat and salt exchange is vigorous due to basal melting and entrainment from the outer region of the ice shelf. In this study, our main findings were summarized in Figure 10. First of all, our hypothesis is the development of two ice front circulations induced by

360 sea ice formation and sub-ice shelf plume. To resolve this, we set the zero velocity at depths from 0 to 280 m, having a no wind effect. Moreover, sea ice formation (1.38 m yr^{-1}) was determined by sensible heat flux which is calculated via wind speed and air temperature observed in AWS. Through this setup, we resolve the ice front circulations in the upper mixed layer. The higher the turbulence intensity, the more ice melting near the ice front occurred. High turbulence intensity causes strong momentum transfer, resulting in increased melting and high-speed currents within the IOBL. The high momentum causes the

365 IOBL current (positive zonal velocity) to flow perpendicular to the ice front after it passes the ice shelf. The horizontal scales of circulations slightly differs for the weak and strong turbulence cases. The horizontal scale of the inner ice front circulation is assumed based on the locations of the local salt maximum at the sea surface (1,776 m for the weak turbulence case and 1,692 m for the strong turbulence case). This denotes that the PISW upwelling and downward force by salt flux are the driving forces of inner ice front circulation. Moreover, PISW upwelling and its accumulation near the sea surface could evidentially support

370 the wedge formation mechanism proposed by Malyarenko et al. (2018). Furthermore, a turbulent Ekman layer developed in all cases, showing that these classical Ekman layers are similar to the non-inclined ice shelf case of Jenkins (2016) in terms of the steady Ekman layer independent of thermal driving broadening. This IOBL current highly interacted with the upper ocean near the ice front, yielding the heterogeneous distribution for the PISW upwelling and freezing rate at the sea surface. This heterogeneous distribution is caused by the baroclinic eddies corresponding to the Rossby radius of deformation and PISW

375 layer near the ice front. Similar to the observation of Naveira Garabato et al. (2017), we also observe the PISW upwelling (gravitational instability) and the development of its baroclinic eddies (centrifugal instability by density gradient) with a strong Ekman layer.

This study employed theoretical power-law profiles of velocity, which have a different turbulence states, because the observation for vertical structures beneath the ice shelf are lacking. In the flux Richardson number in Table 2, no distinct trend

380 exists for the relationship between stratification and turbulence, although we imposed the different turbulence states. This implies that the negative feedback by PISW increases as the turbulence state and its entrainment increases. This study is a preliminary assessment for oceanic structures in a sub-ice shelf environment. The constant model coefficient (C_m) in the SGS

12

model is applied in the IOBL flow near the wall and the flow within the sub-ice shelf plume due to computational cost. This limitation can be solved using a dynamic SGS model, stretched vertical grid and correction of coefficients based on high-resolution DNS results for near-wall physics. The main findings and claimed mechanism of this study can be used to fill the gap in the sub-ice shelf cavity observation. If direct observation for the IOBL flow structures and turbulence characteristics in the sub-ice shelf environment is available, this study can be improved by comparing LES results with observations and their feedback (e.g. correction of ambient values and transfer coefficients). Other important factors that were not included in this study should be addressed and investigated in future studies–e.g., the effect of ice shelf bathymetry (shape and slope) and surface roughness on turbulent characteristics, the temporal variability of the sub-ice water plume, wind stress effect and consideration of the lateral melting at the ice front. A better understanding of the effect of important factors on basal melting and its meltwater dynamics will help in the improvement of the parameterizations (e.g. vertical mixing within the IOBL and sea-ice formation and behavior) in the regional ocean model.

5 Conclusions

We successfully simulated the IOBL flow with a sub-ice shelf plume, the melting effect beneath the NIS, and the freezing effect at the sea surface using a LES model and boundary conditions based on *in situ* observations. Since the inlet profile beneath the ice shelf are hard to observe using *in situ* observation, we assumed that the theoretical power-law profile to describe the different turbulence states. The flow performed for 96 h reaches a quasi-steady state after 14 t^*, exhibiting large fluctuation and a repetitive pattern with temporal convergence. To validate the LES results for four different turbulence states, the simulated zonal velocity, potential temperature, and salinity are compared with 24-h CTD and LADCP observations obtained near the NIS in the Terra Nova Bay of the western Ross Sea in a 2016/2017 shipboard survey. The simulation results agree well with the observations regarding the development of ice front circulations and thermohaline properties. We confirmed that the LES results for both basal melting and freezing effects are realistic through validation with *in situ* observations, implying that the LES model successfully resolves the physical processes occurring in the IOBL. Simulation domain, grid resolution, and turbulence resolving were validated by examining the slope of the one-dimensional energy spectra, the grid sensitivity study to the grid size and magnitude of the SGS fluxes. In the IOBL flow beneath the ice shelf, different turbulence states afforded significantly different features for melting and flow dynamics. In the strong turbulence case, the PISW developed a strong Ekman layer and interacted with the outer ocean, forming heterogeneous patterns for the PISW upwelling and freezing at the sea surface. With increased friction velocity, the melting rate in the strong turbulence case increased by 66% compared to that in the weak turbulence case, maintaining the stratification intensity (flux Richardson number). However, the stratification intensity in the four different turbulence cases did not exhibit a distinct trend, denoting that the stratified forcing by PISW varies according to the flow shear caused by turbulence. This stratification intensity feature should be further investigated by numerical studies of various parameters with state of-the-art observational efforts.

13

References

Arzeno, I. B., Beardsley, R. C., Limeburner, R., Owens, B., Padman, L., Springer, S. R., Stewart, C. R. and Williams, M. J.: Ocean variability contributing to basal melt rate near the ice front of Ross Ice Shelf, Antarctica. J. Geophys. Res. Oceans, 119(7), 4214–4233, doi:10.1002/2014JC009792, 2014.

Begeman, C. B., Tulaczyk, S. M., Marsh, O. J., Mikucki, J. A., Stanton, T. P., Hodson, T. O., Siegfried, M. R., Powell, R. D., Christianson, K. and King, M. A.: Ocean Stratification and Low Melt Rates at the Ross Ice Shelf Grounding Zone, J. Geophys. Res. Oceans, 123(10), 7438–7452, doi:10.1029/2018JC013987, 2018.

Briscolini, M., and Santangelo, P.: Development of the mask method for incompressible unsteady flows. Journal of Computational Physics, 84(1), 57–75, doi:10.1016/0021-9991(89)90181-2, 1989.

Carsey, F. D. and Garwood, Jr. R. W.: Identification of modeled ocean plumes in Greenland Gyre ERS-1 SAR data, Geophys. Res. Lett., 20, 2207-2210, doi:10.1029/93GL01954, 1993.

Coleman, G. N., Ferziger, J. H., Spalart, P. R.: A numerical study of the turbulent Ekman layer. Journal of Fluid Mechanics, 213, 313–348, doi:10.1017/S0022112090002348, 1990.

Davis, P. E., and Nicholls, K. W.: Turbulence observations beneath larsen C ice shelf, Antarctica. J. Geophys. Res. Oceans, 124(8), 5529–5550, doi:10.1029/2019JC015164, 2019.

Denbo, D. W. and Skyllingstad E. D.: An ocean large-eddy simulation model with application to deep convection in the Greenland Sea, J. Geophys. Res.,101, 1095–1110, doi:10.1029/95JC02828, 1996.

Derbyshire, S. H.: Nieuwstadt's stable boundary layer revisited. Quart. J. Roy. Meteor. Soc., 116(491), 127–158, 1990.

Dinniman, M. S., Asay-Davis, X. S., Galton-Fenzi, B. K., Holland, P. R., Jenkins, A. and Timmermann, R.: Modeling ice shelf/ocean interaction in Antarctica: A review, Oceanography, 29(4), 144–153, doi:10.5670/oceanog.2016.106, 2016.

Everett, A., Kohler, J., Sundfjord, A., Kovacs, K. M., Torsvik, T., Pramanik, A., Boehme, L. and Lydersen, C.: Subglacial discharge plume behaviour revealed by CTD-instrumented ringed seals, Sci. Rep., 8(1), 13467, doi:10.1038/s41598-018-31875-8, 2018.

Galton-Fenzi, B. K., Hunter, J. R., Coleman, R., Marsland, S. J., Warner, R. C.: Modeling the basal melting and marine ice
445   accretion of the Amery Ice Shelf. J. Geophys. Res. Oceans, 117(C9), doi:10.1029/2012JC008214, 2012.

Garabato, A. C. N., Forryan, A., Dutrieux, P., Brannigan, L., Biddle, L. C., Heywood, K. J., Jeknins, A., Firing, Y. L., Kimura, S.: Vigorous lateral export of the meltwater outflow from beneath an Antarctic ice shelf. Nature, 542(7640), 219–222, doi.org/10.1038/nature20825, 2017.

Gao, X., Dong, C., Liang, J., Yang, J., Li, G., Wang, D. and McWilliams, J. C.: Convective instability-induced mixing and
450   its parameterization using large eddy simulation, Ocean Model., 137, 40–51, 2019, doi:10.1016/j.ocemod.2019.03.008, 2019.

Gayen, B., Griffiths, R. W. and Kerr, R. C.: Simulation of convection at a vertical ice face dissolving into saline water, J. Fluid Mech., 798, 284–298, doi:10.1017/jfm.2016.315, 2016.

Glendening, J. W.: Horizontally integrated atmospheric heat flux from an Arctic lead, J. Geophys. Res., 100, 4613 – 4621, doi: doi:10.1029/94JC02424, 1995.

455   Gwyther, D. E., Cougnon, E. A., Galton-Fenzi, B. K., Roberts, J. L., Hunter, J. R., and Dinniman, M. S.: Modelling the response of ice shelf basal melting to different ocean cavity environmental regimes, Ann. Glaciol., 57(73), 131–141, doi:10.1017/aog.2016.31, 2016.

Hattermann, T., Nøst, O. A., Lilly, J. M., and Smedsrud, L. H: Two years of oceanic observations below the Fimbul Ice Shelf, Antarctica. Geophysical Research Letters, 39(12), doi:10.1029/2012GL051012, 2012.

460   Heorton, H. D., Radia, N., and Feltham, D. L.: A model of sea ice formation in leads and polynyas. Journal of Physical Oceanography, 47(7), 1701-1718, doi:10.1175/JPO-D-16-0224.1, 2017.

Hewitt, I. J.: Subglacial Plumes. Annual Review of Fluid Mechanics, 52, 145-169, doi:10.1146/annurev-fluid-010719-060252, 2020.

Holland, D. M., Nicholls, K. W. and Basinski, A.: The Southern Ocean and its interaction with the Antarctic Ice Sheet,
465   Science, 367(6484), 1326–1330, doi: 10.1126/science.aaz5491, 2020.

Holland, D. M. and Jenkins, A.: Modeling thermodynamic ice–ocean interactions at the base of an ice shelf, J. Phys. Oceanogr., 29(8), 1787–1800, doi:10.1175/1520-0485(1999)029<1787:MTIOIA>2.0.CO;2, 1999.

Irwin, J. S.: A theoretical variation of the wind profile power-law exponent as a function of surface roughness and stability. Atmos. Environ. (1967), 13(1), 191–194, doi:10.1016/0004-6981(79)90260-9, 1979.

470   Jacobs, S. S., Helmer, H. H., Doake, C. S. M., Jenkins, A. and Frolich, R. M.: Melting of ice shelves and the mass balance of Antarctica, J. Glaciol., 38(130), 375–387, doi:10.3189/S0022143000002252, 1992.

Jackett, D. R., Mc Dougall, T. J., Feistel, R., Wright, D. G., Griffies, S. M.: Algortihms for density, potential temperature, conservative temperature, and the freezing temperature of seawater, J. Atmos. Ocean. Tech., 23, 1709–1728, doi:10.1175/JTECH1946.1, 2006.

15

475   Jenkins, A.: Convection-driven melting near the grounding lines of ice shelves and tidewater glaciers, J. Phys. Oceanogr., 41(12), 2279–2294, doi: 10.1175/JPO-D-11-03.1, 2011.

Jenkins, A.: A simple model of the ice shelf–ocean boundary layer and current. J. Phys. Oceanogr., 46(6), 1785–1803, doi: 10.1175/JPO-D-15-0194.1, 2016.

Jenkins, A., Dutrieux, P., Jacobs, S. S., McPhail, S. D., Perrett, J. R., Webb, A. T. and White, D.: Observations beneath Pine

480   Island Glacier in West Antarctica and implications for its retreat, Nat. Geosci., 3(7), 468–472, doi:10.1038/ngeo890, 2010

Joughin, I., Alley, R. B. and Holland, D. M.: Ice-Sheet Response to Oceanic Forcing. Science, 338(6111), 1172–1176, doi:10.1126/science.1226481, 2012.

Kikumoto, H., Ooka, R., Sugawara, H., Lim, J.: Observational study of power-law approximation of wind profiles within an urban boundary layer for various wind conditions. J. Wind Eng. Ind. Aerod., 164, 13–21, doi:10.1016/j.jweia.2017.02.003,

485   2017.

Kimura, S., Nicholls, K. W., and Venables, E.: Estimation of ice shelf melt rate in the presence of a thermohaline staircase. J. Phys. Oceanogr., 45(1), 133–148, doi:10.1175/JPO-D-14-0106.1, 2015.

Li, B. R., Wang, M. M., Lu, X. Y., Wan, Z. H. and Song, H. E.: Effect of Salinity on Sea Ice Motion. Therm. Sci., 22(4), 1563–1570, doi:10.2298/TSCI1804563L, 2018.

490   Liu, Y., Moore, J. C., Cheng, X., Gladstone, R. M., Bassis, J. N., Liu, H., et al.: Ocean-driven thinning enhances iceberg calving and retreat of Antarctic ice shelves. Proc. Natl. Acad. Sci. 112, 3263–3268, doi:10.1073/pnas.1415137112, 2015.

Maronga, B., Gryschka, M., Heinze, R., Hoffmann, F., Kanani-Sühring, F., Keck, M., Ketelsen, K., Letzel, M. O., Sühring. M. and Raasch, S.: The Parallelized Large-Eddy Simulation Model (PALM) version 4.0 for atmospheric and oceanic flows: model formulation, recent developments, and future perspectives, Geosci. Model Dev., 8, 2515–2551, doi:10.5194/gmdd-8-

495   1539–2015, 2015.

Matsumura, Y. and Ohshima, K. I.: Lagrangian modelling of frazil ice in the ocean, Ann. Glaciol., 56(69) 373–382, doi:10.3189/2015AoG69A657, 2015.

McPhee, M. G., Maykut, G. A. and Morison, J. H.: Dynamics and thermodynamics of the ice/upper ocean system in the marginal ice zone of the Greenland Sea, J. Geophys. Res., 92, 7017–7031, doi:10.1029/JC092iC07p07017, 1987.

500   McConnochie, C. D., and Kerr, R. C.: Dissolution of a sloping solid surface by turbulent compositional convection. J. Fluid Mech, 846, 563–577, doi:10.1017/jfm.2018.282, 2018.

Mondal, M., Gayen, B., and Kerr, R.: Ablation of sloping ice faces into polar seawater. J. Fluid Mech, 863, 545–571, doi:10.1017/jfm.2018.970, 2019

Nicholls, K. W., Abrahamsen, E. P., Buck, J. J. H., Dodd, P. A., Goldblatt, C., Griffiths, G., Heywood, K. j., Hughes, N. E.,

505   Kalezky, A., Lane-Serff, G. F., McPhail, S. D. Millard, N. W., Oliver, K. I. C., Perrett, J., Price, M. R., Pudsey, C. J., Saw, K, Stansfield, K., Stott, M. J., Wadhams, P., Webb, A. T. and Wilkinson, J. P.: Measurements beneath an Antarctic ice shelf using an autonomous underwater vehicle, Geophys. Res. Lett., 33(8), doi:10.1029/2006GL025998, 2016.

Noh, Y., Goh, G., Raasch, S. and Gryschka, M.: Formation of a diurnal thermocline in the ocean mixed layer simulated by LES, J. Phys. Oceanogr., 39(5), 1244–1257, doi:10.1175/2008JPO4032.1, 2009.

510   Petty, A. A., Feltham, D. L. and Holland, P. R.: Impact of atmospheric forcing on Antarctic continental shelf water masses, J. Phys. Oceanogr., 43(5), 920–940, doi:10.1175/JPO-D-12-0172.1, 2013.

Pope, S. B.: Turbulent flows, 2001.

Raasch, S. and Schröter, M.: PALM–a large-eddy simulation model performing on massively parallel computers, Meteorol. Z., 10(5), 363–372, doi:10.1127/0941-2948/2001/0010-0363, 2001.

515   Ramudu, E., Gelderloos, R., Yang, D., Meneveau, C. and Gnanadesikan, A.: Large eddy simulation of heat entrainment under arctic sea ice, J. Geophys. Res. Oceans, 123, 287–304, doi:10.1002/2017JC013267, 2018.

Rees Jones, D. W., Wells, A. J.: Frazil-ice growth rate and dynamics in mixed layers and sub-ice-shelf plumes. Cryosphere, 12(1), 25–38, doi:10.5194/tc-12-25-2018, 2018.

Rignot, E., Jacobs, S., Mouginot, J. and Scheuchl, B.: Ice-shelf melting around Antarctica, Science, 341(6143), 266–270,
520   doi:10.1126/science.1235798, 2013.

SeaBird Electronics, Inc.: Seasoft V2: SBE data processing (User's Manual, pp. 1–174). Bellevue, Washington, USA, 2014.

Sharqawy, M. H., Lienhard, J. H. and Zubair, S. M.: Thermophysical properties of seawater: a review of existing correlations and data. Desalination and water treatment, 16(1–3), 354–380, doi:10.5004/dwt.2010.1079, 2010.

Skyllingstad, E. D. and Denbo, D. W.: Turbulence beneath sea ice and leads: a coupled sea ice/large eddy simulation study,
525   J. Geophys. Res., 106(C2), 2477–2497, doi:10.1029/1999JC000091, 2001.

Smith, B., Fricker, H. A., Gardner, A. S., Medley, B., Nilsson, J., Paolo, F. S., Holschuh, N., Adusumilli, S., Brunt, K., Csatho, B., Harbeck, K., Markus, T., Neumann, T., Siegfried, M. R., and Zwally, H. J.: Pervasive ice sheet mass loss reflects competing ocean and atmosphere processes. Science, eaaz5845, doi:10.1126/science.aaz5845, 2020.

Stanton, T. P., Shaw, W. J., Truffer, M., Corr, H. F. J., Peters, L. E., Riverman, K. L., Bindschadler, R., Holland, D. M., and
530   Anandakrishnan, S.: Channelized Ice Melting in the Ocean Boundary Layer Beneath Pine Island Glacier, Antarctica. Science, 341(6151), 1236–1239, doi: 10.1126/science.1239373, 2013.

Stevens, C., Lee, W. S., Fusco, G., Yun, S., Grant, B., Robinson, N. and Hwang, C. Y.: The influence of the Drygalski Ice Tongue on the local ocean, Ann. Glaciol., 58(74), 51–59, doi:10.1017/aog.2017.4, 2017.

Thompson, L., Smith, M., Thomson, J., Stammerjohn, S., Ackley, S., and Loose, B.: Frazil ice growth and production during
535   katabatic wind events in the Ross Sea, Antarctica. Cryosphere, 14(10), 3329–3347, doi:10.5194/tc-14-3329-2020, 2020.

Thurnherr, A. M.: How to Process LADCP Data with the LDEO Software. New York: Columbia University. ftp://ftp.ldeo.columbia.edu/pub/LADCP/HOWTO/LDEO_IX.pdf, 2014.

Vreugdenhil, C. A., and Taylor, J. R.: Stratification effects in the turbulent boundary layer beneath a melting ice shelf: Insights from resolved large-eddy simulations, J. Phys. Oceanogr., 49(7), 1905–1925, doi:10.1175/JPO-D-18-0252.1, 2019.

540   Wicker, L. J. and Skamarock, W. C.: Time-splitting methods for elastic models using forward time schemes, Mon. Weather Rev., 130(8), 2088–2097, doi:10.1175/1520-0493(2002)130<2088:TSMFEM>2.0.CO;2, 2002.

Wray, P. A.: Spatial analysis of the Nansen ice shelf basal channel, using ice penetrating radar (Master's thesis, University of Waterloo), 2019.

545 Yoon, S. T., Lee, W. S., Stevens, C., Jendersie, S., Nam, S., Yun, S., Hwang, C. Y., Jang, G. I., and Lee, J.: Variability in high-salinity shelf water production in the Terra Nova Bay polynya, Antarctica, Ocean Sci., doi:10.5194/os-16-373-2020, 2020.

550

555

Table 1. List of model parameters and constants

λ_1	Freezing temperature salinity coefficient	-0.0573	$°C\ kg\ g^{-1}$
λ_2	Freezing temperature constant	0.0832	$°C$
λ_3	Freezing temperature depth coefficient	-7.53×10^4	$°C\ m^{-1}$
Γ_S	Salt turbulent exchange coefficient (sea surface, ice shelf bottom)	2×10^{-4} [a], 2.6×10^{-4} [b]	-
Γ_θ	Heat turbulent exchange coefficient (sea surface, ice shelf bottom)	5.8×10^{-3} [a], 8×10^{-3} [b]	-
c_w	Specific heat capacity of pure water	3974	$J\ kg^{-1}°C^{-1}$
L_i	Latent heat of fusion	3.35×10^5	$J\ kg^{-1}$
ρ_w	Density of water	1028	$kg\ m^{-3}$
ρ_i	Density of ice	917	$kg\ m^{-3}$
z_0	Surface roughness (sea surface, ice shelf bottom)	$0.001, 0.005$ [c]	m
-	Ice shelf thickness	280 [d]	m
θ_f	Local freezing temperature (sea surface, ice shelf bottom)	$-1.9, -2.115$	$°C$
θ_a	Ambient temperature (sea surface, ice shelf bottom)	$-1.9, -2.06$	$°C$
θ_b	Interfacial temperature (sea surface, ice shelf bottom)	$-1.879, -2.092$	$°C$
Sa_a	Ambient salinity (sea surface & ice shelf bottom)	34.69	Psu
Sa_b	Interfacial salinity (sea surface, ice shelf bottom)	$34.9425, 34.286$	Psu

k_θ	molecular diffusivities of heat	1.3×10^{-7}	$m^2\ s^{-1}$
k_S	molecular diffusivities of salt	7.2×10^{-10}	$m^2\ s^{-1}$
u_*	Friction velocity (sea surface, ice shelf bottom)	0.026, calculated	$m\ s^{-1}$
	Wind speed, air temperature in AWS	16.23, −7.76	$m\ s^{-1}$, °C
Q_s	Sensible heat flux at sea surface	164.88[e]	$W\ m^{-2}$
F	Frazil ice formation	1.38[e]	cm day^{-1}

a – **Heorton et al. (2017)**

b – **based on friction velocity (0.168 m s^{-1}) and thermal driving (refer to Vreugdenhil and Taylor (2019))**

c – **Smooth ice with melting case ($C_d = 0.001$) in Gwyther et al. (2016)**

560   d – **Stevens et al. (2017)**

e – **Thompson et al. (2020)**

Table 2. Main values of four different cases ($Ri_f = \frac{\frac{g}{\rho_{\theta,0}}(\overline{\rho_\theta' w'})}{-\overline{u'w'}(\frac{\partial U}{\partial z})}$)

| Case	Friction velocity at ice shelf (m s^{-1})	IOBL depth (m)	Large eddy turnover time, t* (hour)	Averaged melt rate (m yr^{-1})	Averaged freezing rate (m yr^{-1})	Flux Richardson number, Ri_f
n=3	0.001686	30	4.94	0.092	2.628	0.0464
n=4	0.002077	33	4.41	0.109	2.72	0.0418
n=5	0.002548	36	3.93	0.139	2.671	0.0599
n=7	0.002765	39	3.92	0.153	3.142	0.0378

Figure 1: Region of interest and simulation domain configuration. (a) Map of Antarctica. The red box shows the study area of Terra Nova Bay in the western Ross Sea. (b) Region of interest where conductivity-temperature-depth (CTD) and lowered acoustic Doppler current profiler (LADCP) surveys were conducted in the 2016/17 shipboard survey. (c) Simulation domain and boundary conditions.

565

Figure 2: Time series of friction velocities in four cases. The total time (96 h) was normalized by each large-eddy turnover time, t^*, which was calculated by overturning eddy scale (ice shelf-ocean boundary layer (IOBL) scale) divided by the friction velocity. The inset figure shows four different theoretical profiles of velocity.

570
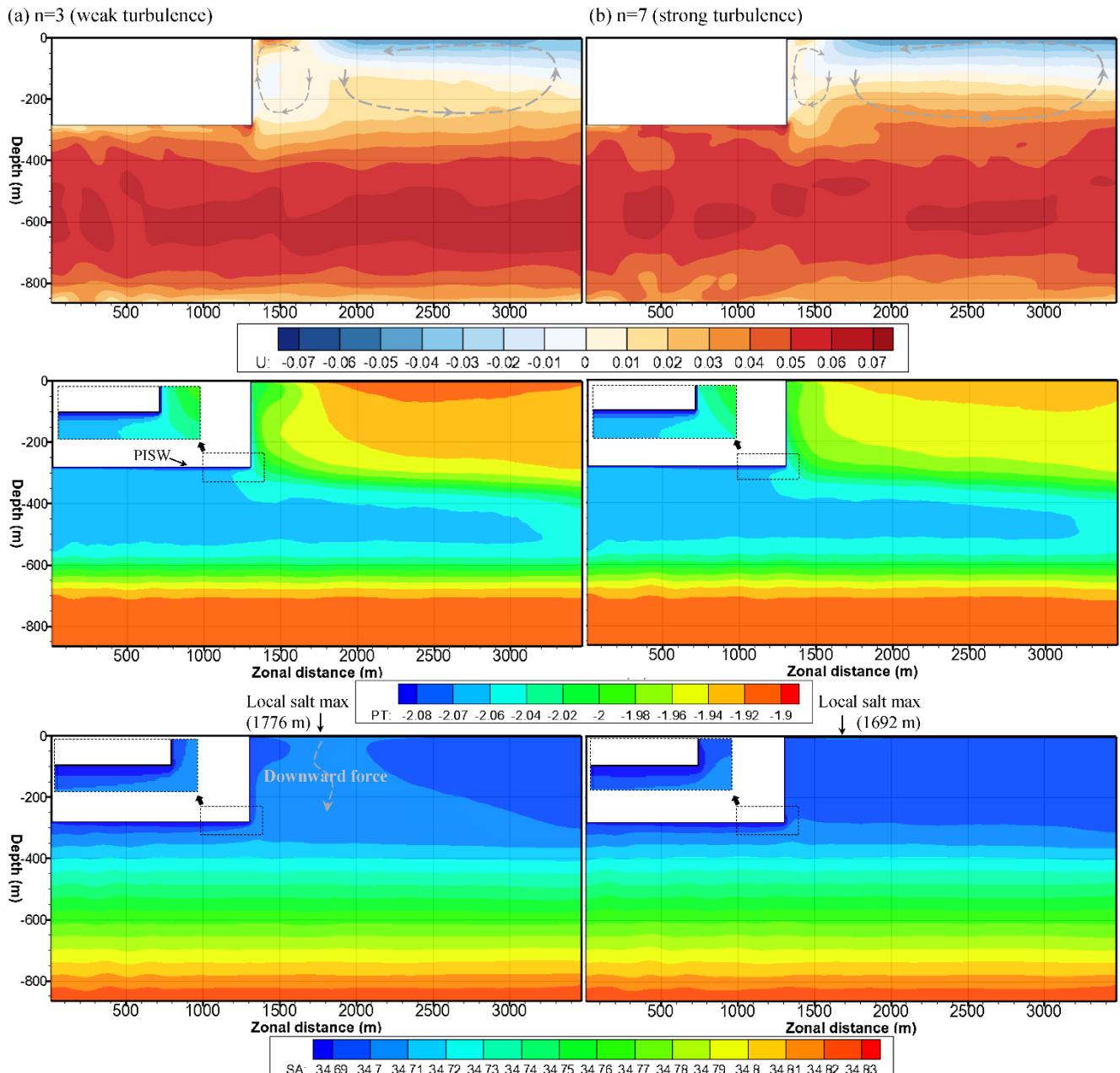
Figure 3: XZ cross-section contours (y = 1,728 m, domain center) of zonal velocity, potential temperature, and salinity in the n = 3 (left) and n = 7 (right) cases. In these contours, the zonal direction is perpendicular to the ice shelf front. These results were time-averaged in the last 3 t* period. Upper panel: zonal velocity, middle panel: potential temperature and lower panel: salinity.
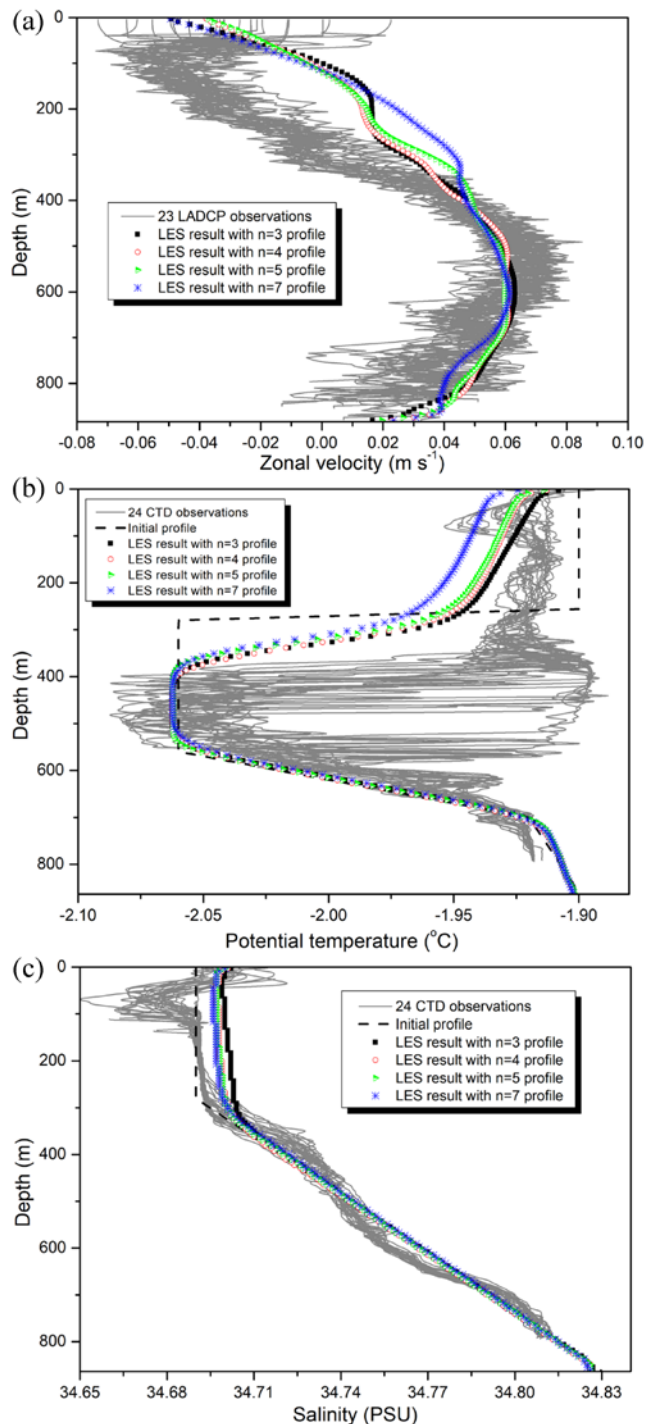
Figure 4: Vertical profiles of velocity, potential temperature, and salinity from the CTD and LADCP observations (solid grey lines), initial profiles (black dashed line), and the results of the large-eddy simulation (LES). (a) zonal velocity. (b) potential temperature. (c) salinity.
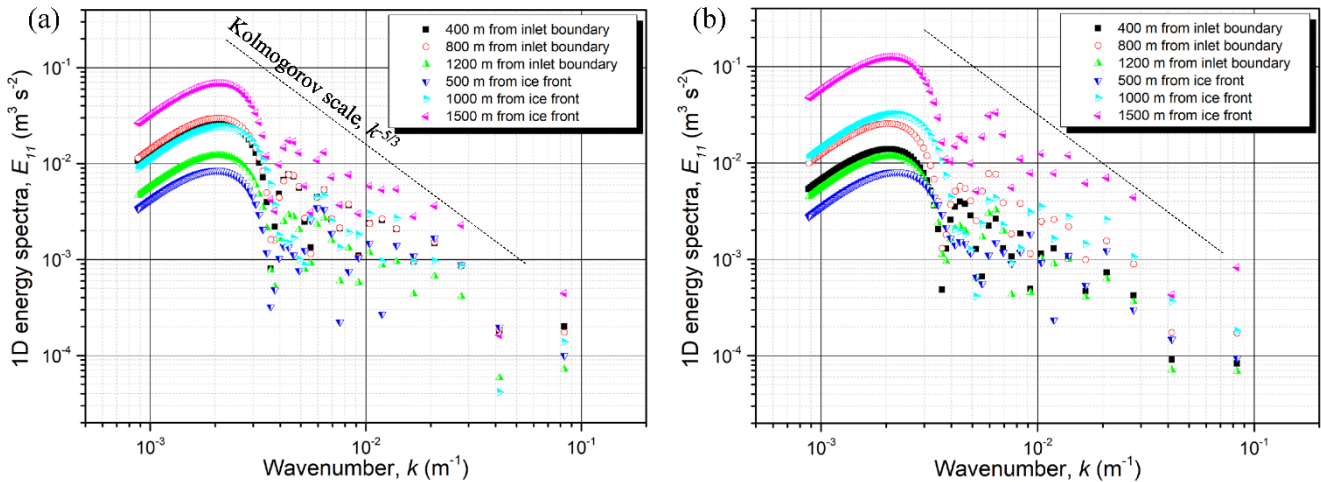
Figure 5: One-dimensional turbulence energy spectra at the depth of the positively-buoyant, ice shelf water (PISW) center (291 m depth) within IOBL. (a) n = 3 and (b) n = 7. Different shapes and colors represent the values at different zonal distances: 400, 800, 1200, 1800, 2300 and 2800 m.
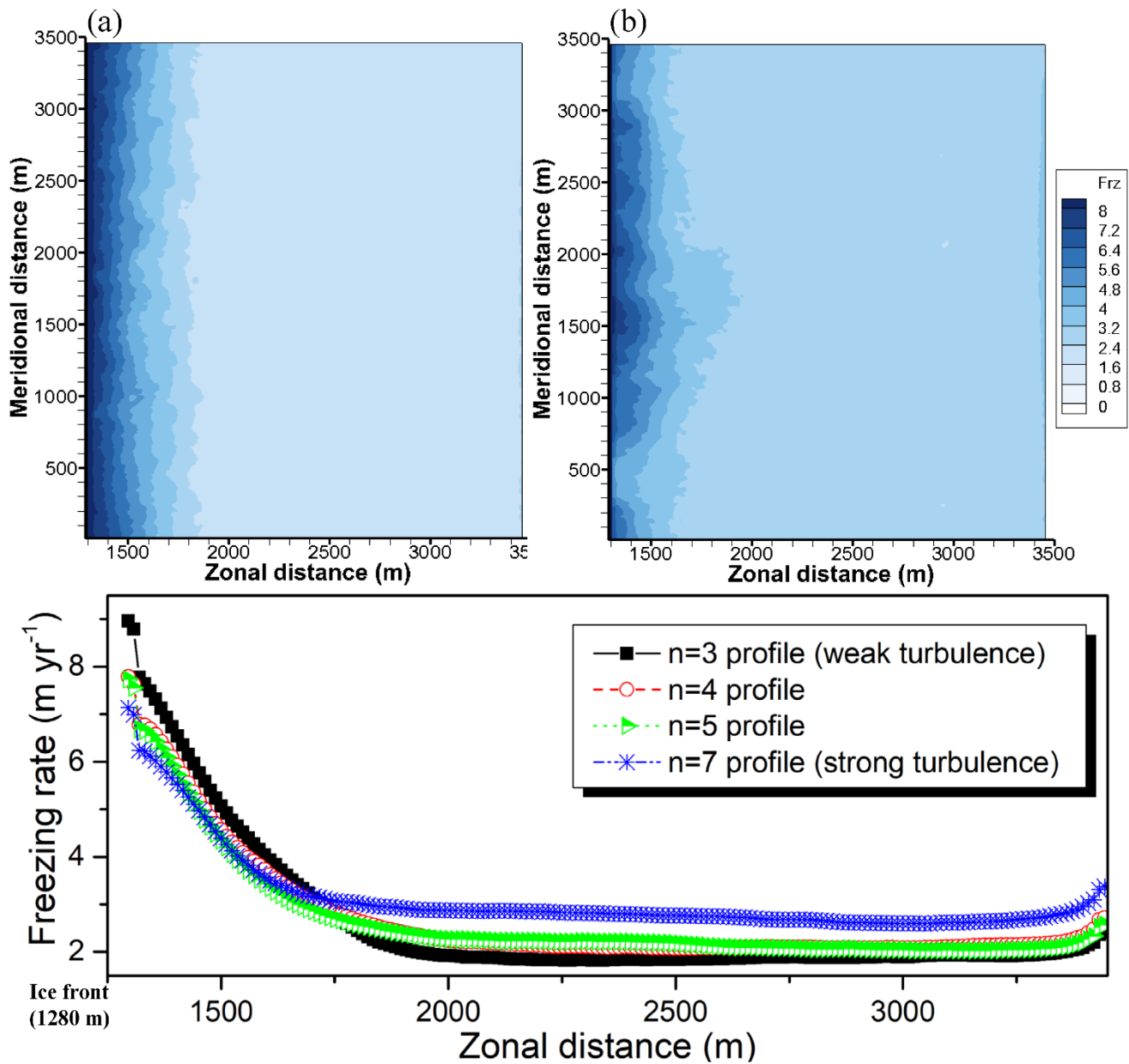
Figure 6: XY horizontal distribution of 3 t[*] time-averaged freezing rate (m yr^{-1}) at the sea surface. (a) n = 3, weak turbulence. (b) n = 7, strong turbulence (c) Zonally-spatial distribution of freezing rate in four different turbulence cases. These values are averaged along the meridional direction.

590
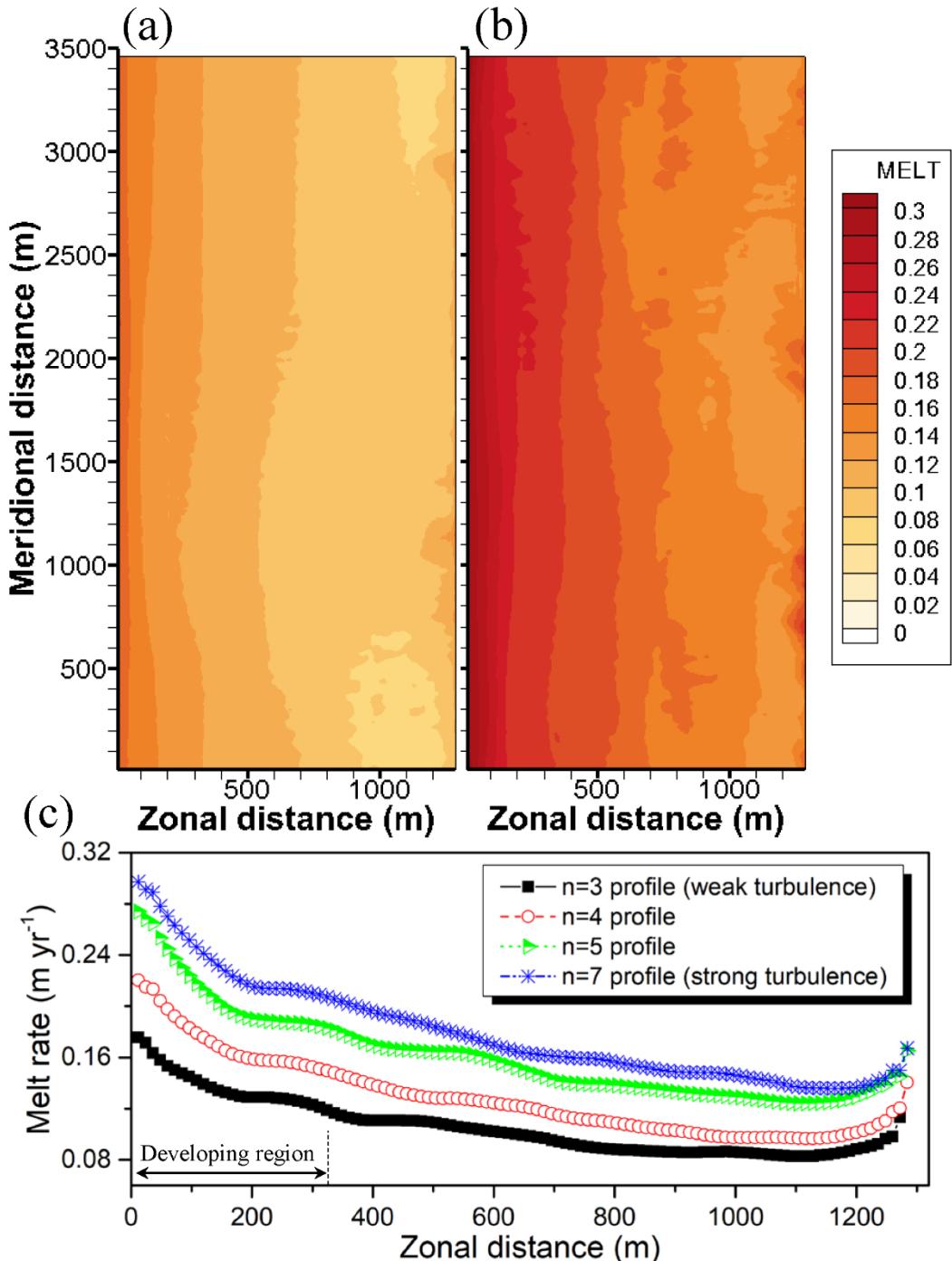
Figure 7: XY horizontal distribution of 3 t* time-averaged melting rate (m yr⁻¹) at ice shelf base (280 m). (a) n = 3, weak turbulence. (b) n = 7, strong turbulence (c) Zonally-spatial distribution of the melting rate in four different turbulence cases. These values are averaged along the meridional direction.
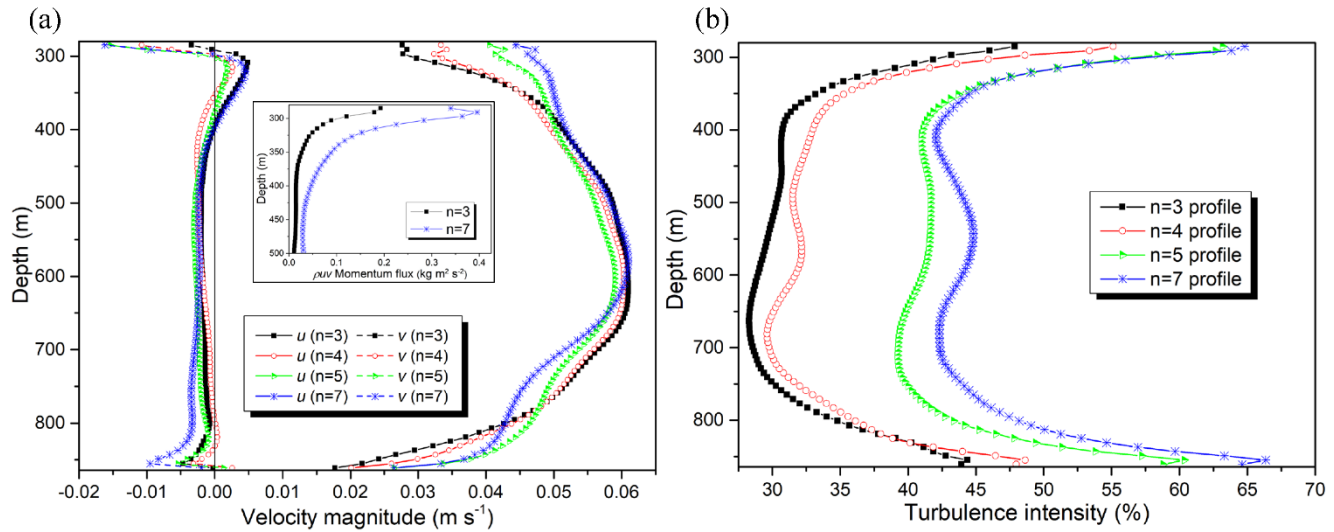
Figure 8: Vertical profiles of (a) *u*, *v* mean velocities and (b) turbulence intensity. The inset in (a) is about the vertical profile of horizontal momentum flux for the Ekman layer formation beneath the ice shelf.
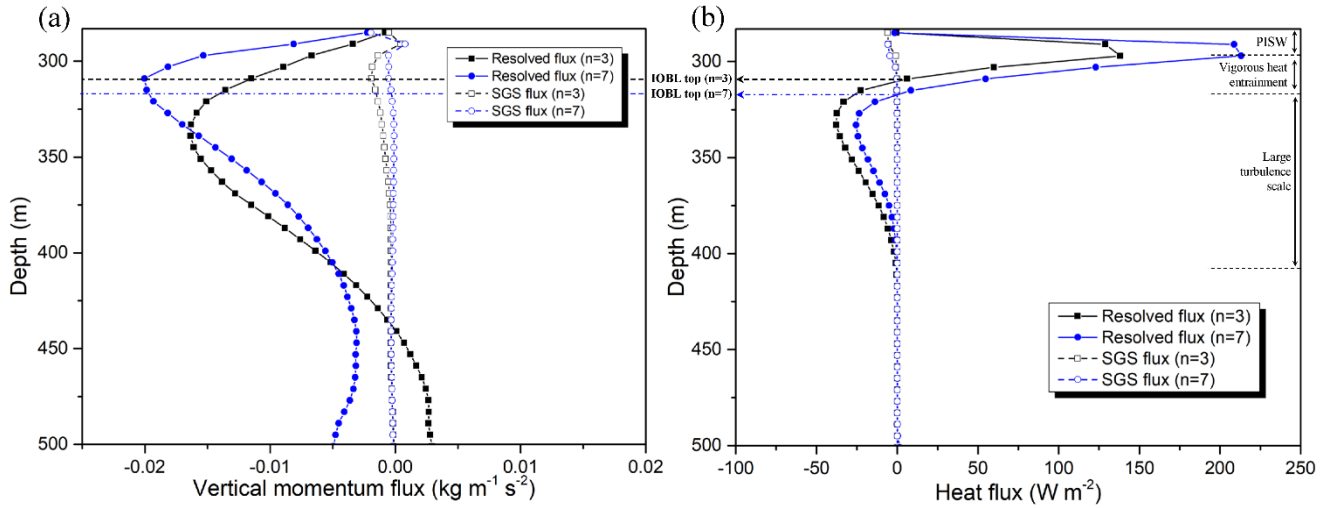
Figure 9: Vertical profiles of momentum fluxes and heat fluxes. Fluxes were characterized using resolved flux and subgrid scale (SGS) flux. (a) Momentum fluxes (resolved: $\rho_0 \overline{u'w'}$, SGS: $\rho_0 K_m \partial \overline{u}/\partial z$). (b) Heat fluxes (resolved: $\rho_0 c_s \overline{w'\theta'}$, SGS: $\rho_0 c_s K_h \partial \overline{\theta}/\partial z$, where ρ_0 (1024 kg m^{-3}) is the reference density of seawater, and c_s (4.02 × 10^3 J kg^{-1} K^{-1}) is the specific heat capacity of seawater (Sharqawy et al., 2010)).
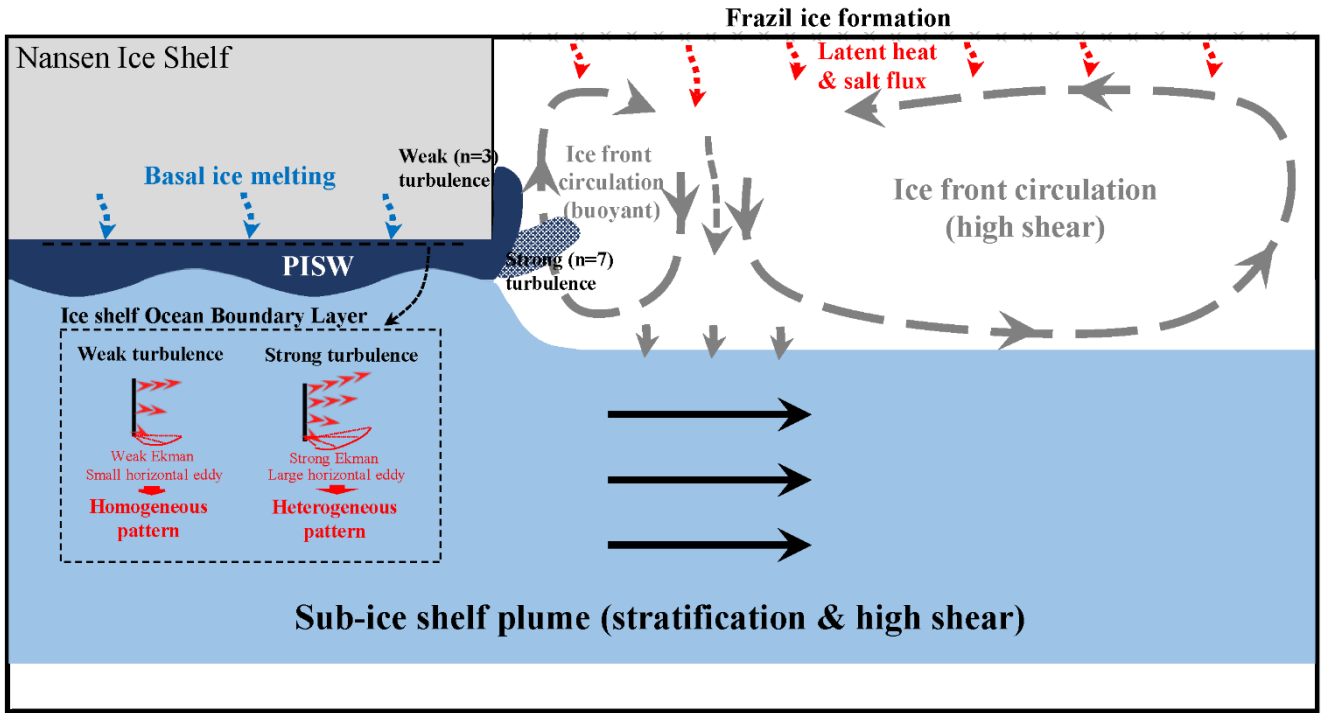
Figure 10: Final conclusions and schematic diagram for oceanography near the ice front of NIS and various physics within IOBL resolved by LES.